CLIMATOLOGY

Increased occurrences of early Indian Ocean Dipole under global warming

Shuangwen Sun[1,2,3], Yue Fang[1,2,3]*, Yongcan Zu[1,2,3], Lin Liu[1,2,3], Kuiping Li[1,2,3]

The Indian Ocean Dipole (IOD) is a prominent mode of ocean-atmosphere interannual variability with great climate and socioeconomic impacts. Early positive IOD (pIOD), a newly discovered type of pIOD, induces pronounced rainfall anomalies in boreal summer more than canonical pIOD. It also contributes to more frequent consecutive pIODs, causing devastating droughts and floods. How early pIOD responds to global warming remains unknown. Here, we show that early pIOD has increased substantially in the past decades, reaching the same frequency as canonical pIOD. The increase is caused by intensified Bjerknes feedback and an early summer monsoon onset, which is the major trigger for early pIOD. Model simulations suggest that the increased frequency of early pIOD is likely to continue under greenhouse warming by the same mechanisms as in the observations, increasing boreal summer climate variability and leading to more climate extremes in affected regions.

INTRODUCTION

The Indian Ocean Dipole (IOD) is a prominent mode of air-sea interaction in the tropical Indian Ocean. During a positive IOD (pIOD) event, the sea surface temperature (SST) is anomalously cool in the southeastern Indian Ocean and anomalously warm in the western Indian Ocean, accompanied by pronounced anomalous easterlies over the central equatorial Indian Ocean and anomalous southeasterly along the coast of Sumatra (1). The IOD is a substantial source of interannual climate variability across the globe. Convection anomalies associated with pIOD cause droughts in East Asia, Australia, and the Arabian Peninsula and flooding to parts of India and East Africa (1–7). Anomalies of sea level and upwelling intensity during pIOD have an important impact on the regional biological productivity (8). In addition, wildfires associated with the severe droughts caused by pIOD events affect the global carbon budget as well (9). Owing to its large climate and societal and economic impacts, the IOD has received wide research interest ever since it was discovered in 1999.

The pIOD displays strong diversity in spatial pattern and intensity and seasonal cycle (10–16). There is a previously unidentified type of pIOD, which appears more after the mid-1970s (13, 15), featuring a similar spatial pattern to a canonical pIOD but with distinct seasonal-locking characteristics. A canonical pIOD develops in boreal summer and peaks in fall, but the newly identified type of the pIOD develops in boreal spring and matures in summer (13). As a result, it is referred to as early pIOD [also unseasonable pIOD in previous work (13)]. Although a pIOD often interacts and frequently occurs with El Niño/Southern Oscillation (ENSO) (17–19), some pIOD events occur without ENSO (8, 20–22). Early pIOD is a climate mode inherent to the tropical Indian Ocean (13) and is tightly linked to anomalous Indian monsoon activities in boreal spring (15). The seasonality of early pIOD is consistent with the equatorial mode in the Indian Ocean, which also becomes active under global warming (23). It is reported that pIOD is projected to be stronger during boreal summer in the near future, suggesting an early onset of pIOD events (24).

Such early pIOD events drive rainfall and salinity and temperature anomalies with similar spatial patterns as that induced by canonical pIOD events (16, 25). The precipitation anomalies associated with an early pIOD appear one season earlier than during a canonical pIOD (14), thus increasing climate variability in summer. Moreover, early pIOD events contribute to an increased frequency of pIOD events over the past decades, leading to divergent east-west trends in rainfall across the Indian Ocean basin, inducing drought in western Indonesia and southeastern Australia and heavy rains over eastern Africa and southern India (4). The early pIOD events disturb the biennial tendency of canonical pIOD events (18), causing more frequent consecutive pIOD events. Consecutive pIOD events occurred only once in the last century but have already appeared two times since 2000 (Fig. 1A). The rainfall anomalies accumulated during the years of consecutive pIOD events result in recording-breaking SST and rainfall fluctuations, including devastating wildfires, droughts, and flooding in the Indian Ocean rim countries (26–28).

These marked impacts of early pIOD call for an investigation into why it has increased in the past decades and how its frequency will change in a warming climate. Here, we show that the increased occurrences of early pIOD events in recent decades are related to an early summer monsoon onset and enhanced Bjerknes feedback. In addition, the Coupled Model Intercomparison Project [CMIP5 (29) and CMIP6 (30)] simulations show that these early pIOD events will likely become more frequent under future greenhouse warming by the same mechanisms as in the observations.

RESULTS

Differences between early pIOD and pIOD co-occurring with ENSO

The similar east-west dipole pattern of SST anomalies (SSTAs) means that early pIOD cannot be distinguished from canonical

[1]First Institute of Oceanography and Key Laboratory of Marine Science and Numerical Modeling, Ministry of Natural Resources, Qingdao 266061, China. [2]Laboratory for Regional Oceanography and Numerical Modeling, Pilot National Laboratory for Marine Science and Technology, Qingdao 266237, China. [3]Shandong Key Laboratory of Marine Science and Numerical Modeling, Qingdao 266061, China.
*Corresponding author. Email: yfang@fio.org.cn
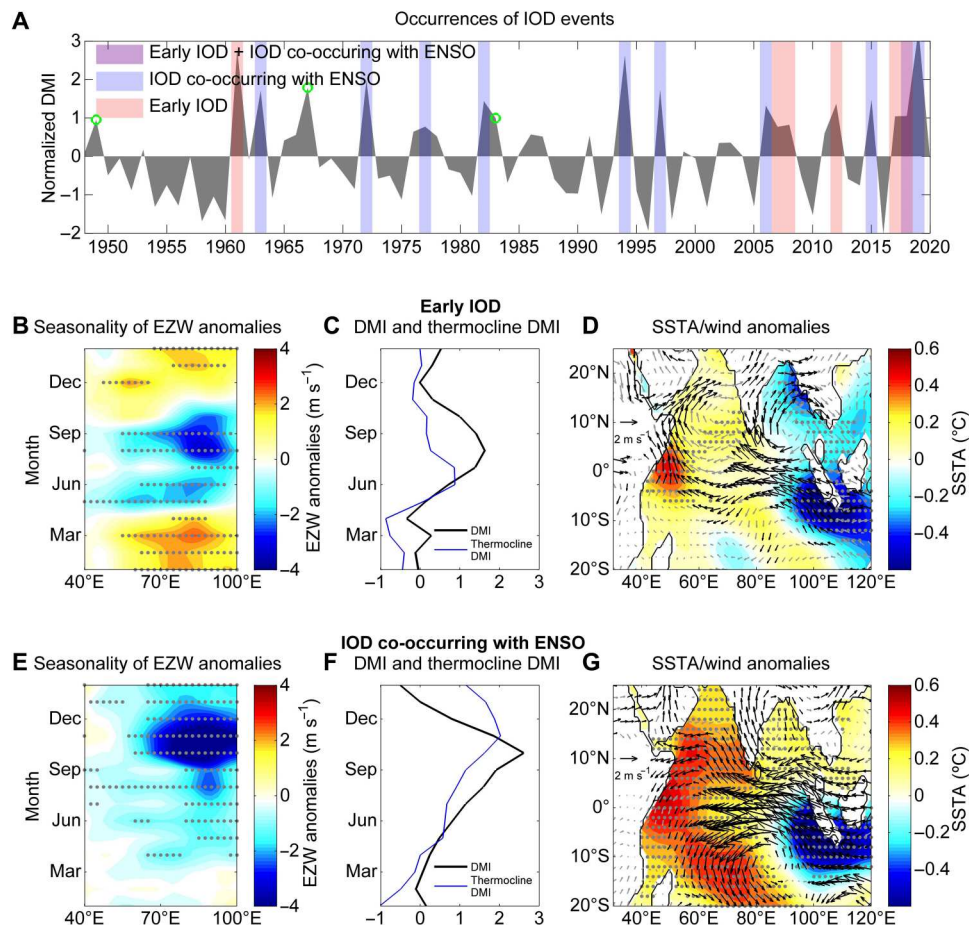
Fig. 1. Observed characteristics of early pIOD and pIOD co-occurring with ENSO. (**A**) The normalized time series of dipole mode index (DMI) with linear trend being removed (averaged between July and October; gray shading). The blue vertical bars indicate pIOD events co-occurring with ENSO (the DMI and Niño 3.4 index are both greater than 0.75 SD). The red bars indicate early pIOD events [the DMI and the principal component (PC) of spring-summer equatorial easterly wind anomaly (EEWA) mode are both greater than 0.75 SD]. The purple bar indicates that pIOD co-occurring with ENSO coincides with early pIOD in the same year. The pIOD events that are neither pIOD co-occurring with ENSO nor early pIOD are indicated by green circles. (**B**) Composite seasonal evolutions of equatorial zonal wind (EZW; averaged between 5°S and 5°N; m s^{-1}) anomalies. (**C**) Composite DMI (SD; thick line) and thermocline DMI (SD; thin line) calculated using a normalized time series of DMI and thermocline DMI for early pIOD events. (**D**) Composites of SST anomalies (SSTA) (°C; color shading) and 850-hPa wind anomalies (m s^{-1}; vectors) in the peak month (August) of early pIOD events. Wind vectors that exceed the 90% confidence level are shown in black, while others are shown in gray. (**E** and **F**) Same as (B) and (C), but for pIOD events co-occurring with ENSO. (**G**) Same as (D), but in the peak month (October) of pIOD events co-occurring with ENSO. Linear trends of SSTA and wind anomalies are removed before the composition. Values that exceed 90% confidence level are indicated by gray dots.

pIOD by just the dipole mode index (DMI) (*1*). Considering that coupling between IOD intensity and equatorial zonal wind anomalies is a fundamental feature of the IOD (*1*), we use the first two dominant empirical orthogonal function (EOF) modes of month-reliant equatorial zonal wind variability, which are independent from each other, to differentiate these two types of pIOD events (*15*). In the EOFs, the two-dimensional "spatial" part is the seasonal evolution of equatorial zonal wind anomalies of individual years, and the "temporal" dimension is the years from 1948 to 2020 (see the "EOF analysis" section and figs. S1 and S2).

The most notable feature of the first leading mode (EOF1) is that the equatorial easterly wind anomalies (EEWAs; EOF1 is also referred to as the fall EEWA mode) peak in boreal fall, corresponding to the EEWA variation during a canonical pIOD. In the second leading mode (EOF2; also referred to as the spring-summer EEWA mode), the EEWA set up in May and persist through

boreal spring and summer, which is consistent with the EEWA evolution during an early pIOD event (figs. S1 and S2). The regressed thermocline depth anomalies and DMI onto the principal components (PCs) of these two modes depict the key characteristics of canonical and early pIOD events (fig. S3).

We examine pIOD events over the period from 1948 to 2020. We select pIOD events when the DMI exceeds 0.75 SD. An early pIOD is defined as a DMI and the second PC (PC2) both greater than 0.75 SD, while pIOD co-occurring with ENSO is defined as a DMI and the Niño 3.4 index both greater than 0.75 SD (see the "Occurrences of pIOD events" section). Under these criteria, in total, 18 significant pIOD events are identified (Fig. 1A). Among them, 10 are pIOD events co-occurring with ENSO and 6 are early pIOD events. There is one pIOD event that occurs with both ENSO and spring-summer EEWA in the same year. Therefore, pIOD events co-occurring with ENSO and early pIOD events are the two

dominant types of pIOD events; they account for the vast majority (83.3%) of all pIOD events.

Compared with pIOD events co-occurring with ENSO, there are some notable distinct features in early pIOD events. First, in early pIOD events, the EEWA develops abruptly in May. The intensity of EEWA reaches 2 m s^{-1} within less than a month (Fig. 1B). In contrast, the EEWA during pIOD events co-occurring with ENSO remains weak in boreal spring and summer; then, it intensifies rapidly in September and reaches its peak in boreal fall (Fig. 1E). Second, the spatial patterns of wind anomalies are distinct in these two types of pIOD events (Fig. 1, D and G). The wind anomaly is confined to the equatorial and northern Indian Ocean during early pIOD events and exhibits a summer monsoon–like pattern. In contrast, the EEWA is accompanied by a pronounced anticyclone over the southern Indian Ocean during pIOD events co-occurring with ENSO. Third, the duration of dipole anomalies in SST and thermocline depth is generally consistent during early pIOD events; however, the DMI peaks 2 months earlier than the thermocline DMI during pIOD events co-occurring with ENSO (Fig. 1, C and F; see the "Occurrences of pIOD events" section).

These distinct features can be understood by considering the different forcing mechanisms of the two types of pIOD events. Early pIOD events are triggered by anomalously early onset of the Indian summer monsoon. Significant EEWA is established about 2 weeks after the monsoon onset in the Bay of Bengal (BoB), which is in mid-May (15). As described by Sun et al. (15), in years with early monsoon onset, the convection is anomalously enhanced in the BoB during late April to early May. Anomalous westerlies in a band between 0° and 15°N intensify as a response to the anomalous convective latent heat release, contributing to an early monsoon onset. Subsequently, suppressed convection is seen in the southwestern Indian Ocean in late April and gradually intensifies as its center propagates eastward. Meanwhile, the 850-hPa wind anomalies move in concert with the outgoing longwave radiation (OLR) anomalies and manifest themselves as a Rossby wave response to the corresponding anomalous convective heating (31). In the

third pentad of May, the anomalously suppressed convection becomes strongest and arrives at the eastern equatorial Indian Ocean. Under this situation, a significant easterly anomaly is established in the equatorial Indian Ocean.

That is why the wind anomalies associated with early pIOD develop rapidly in May and show a monsoon-like pattern. These wind anomalies induce cooling in the eastern Indian Ocean through upwelling, cold advection, and enhanced evaporation and induce warm advection to the western Indian Ocean (15). Then, the initial SSTA and wind anomalies grow under Bjerknes feedback in the following months and reach their peak in August. In the absence of persistent external forcing, early pIOD events decay in fall, when pIOD events co-occurring with ENSO peak (table S1).

During pIOD events co-occurring with ENSO, wind anomalies are remotely forced by the Pacific Ocean. They gradually intensify as ENSO grows from boreal summer to fall, generating the phase-locking feature of pIOD co-occurring with ENSO (17, 32). In the decay phase of pIOD events co-occurring with ENSO, ENSO induced changes in surface heat flux, particularly the solar radiation, contributing to an abrupt warming in the SST of the equatorial eastern Indian Ocean. The dipole pattern of SSTA switches to a basin-wide warming pattern in the Indian Ocean (3, 33). The thermocline depth anomalies are not directly influenced by the surface heat flux and, thus, persist longer than the SSTA dipole, leading to the different peaking time of the DMI and the thermocline DMI during pIOD events co-occurring with ENSO. Therefore, the early pIOD and pIOD co-occurring with ENSO are different not only in their seasonality but also in their triggering and development mechanisms.

Decadal variability of early pIOD
We analyzed the decadal changes in the frequency of all pIOD events and the frequency of the two types of pIOD events separately (Fig. 2A). The occurrences of pIOD events co-occurring with ENSO have increased before the 1990s. pIOD co-occurring with ENSO is the dominant type of pIOD in this period, and the EEWA is strongly
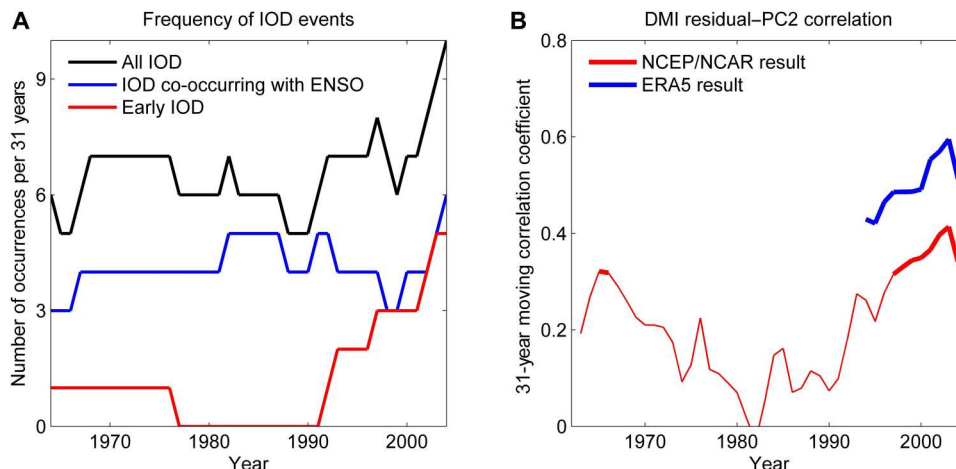
Fig. 2. Observed intensification of early pIOD events in recent decades. (**A**) Number of observed pIOD events in 31-year sliding periods (black line). The blue line indicates that of pIOD events co-occurring with ENSO and the red line indicates that of early pIOD events. (**B**) Thirty-one–year moving correlation between ENSO-independent residuals of the DMI and time series of spring-summer EEWA mode (PC2). Red and blue lines indicate that the PC2 used for correlation analysis is calculated on the basis of National Centers for Environmental Prediction/National Center for Atmospheric Research (NCEP/NCAR) and ERA5 reanalysis, respectively. Results over 90% confidence level are thickened.

correlated with ENSO in these years (*22*). However, after the 1990s, the frequency of pIOD events co-occurring with ENSO has remained stable, but the frequency of early pIOD events has increased substantially. The frequency of early pIOD events has increased to 5 per 31 years, which is comparable to that of pIOD events co-occurring with ENSO. The marked change in the frequency of pIOD events after the 1990s is mainly attributed to the increase of early pIOD events.

To further analyze the contribution of early pIOD events to DMI variations, we constructed residual records of the ENSO-independent pIOD events by removing the common influence of ENSO (see the "Occurrences of pIOD events" section). The 31-year running correlation between PC2 and the IOD residual time series is insignificant before the 1990s but continued to grow in recent decades and became significant in the mid-1990s (Fig. 2B). Now, the spring-summer EEWA mode has become a key influencing factor for DMI. Consequently, early pIOD events, which are closely related to the spring-summer EEWA mode, have become a major type of pIOD events.

The above analysis shows that not only the frequency of pIOD events has changed but also the composition of pIOD events has changed since the 1990s. pIOD events co-occurring with ENSO were the only dominant type of pIOD events in the past, but after the 1990s, the type of early pIOD has also become a major part of the pIOD events.

Causes for the increased occurrences of early pIOD

Early pIOD events are triggered by anomalously early onset of summer monsoon and maintained by the Bjerknes feedback. We find that the increased occurrences of early pIOD in the past decades are also related to these two factors.

First, the trigger for early pIOD events has become more active in recent decades. It is reported that the monsoon onset over the BoB tends to be earlier during the past decades (*34*, *35*). Therefore, the atmospheric anomalies associated with the early monsoon onset, including the spring EEWA, occur more frequently. This is conductive to the increase of early pIOD events. This is consistent with the previous finding that Indian summer monsoon could modulate decadal IOD variations (*5*).

In particular, the BoB convection center is the principal heat source in driving the south Asian summer monsoon (*36*). The onset of south Asian summer monsoon starts with the development of strong convection over the BoB around late April and early May (*37*, *38*). The BoB convection (as indicated by the OLR) during the monsoon onset stage has been strengthening in the past decades, implying that the development of BoB convection is getting earlier (*38*). On decadal time scales, the BoB OLR is correlated with the monsoon onset date (see the "Monsoon onset date" section) at 0.86, which is significant above the 95% confidence level (Fig. 3A).

Meanwhile, the atmosphere has become more sensitive to the variations in convection. The correlation between BoB convection anomalies and EEWA in May has enhanced markedly in recent decades (Fig. 3B). The correlation coefficient was below significance before the mid-1990s but rose considerably afterward. The increased ocean-land temperature difference in boreal spring under global warming provides a favorable condition for summer monsoon to be triggered (*39*). This explains why the atmosphere has become more responsive to the convection anomalies. In

addition, the EEWA can persist longer after they are triggered. Compared to the 1990s, the duration of EEWA increases by about 2 months after 2005 (Fig. 3B). This indicates that not only the triggering mechanism but also the maintaining mechanism for early pIOD has also enhanced. Considering that Bjerknes feedback is essential for the maintenance and growth of the original anomaly signal, we then examine the decadal variation in the strength of Bjerknes feedback.

The Bjerknes feedback processes include the SST response to the thermocline variation, the equatorial zonal wind response to SST, and the thermocline response to the equatorial zonal wind (*40*). The overall Bjerknes feedback strength is determined by the combined effect of these three processes (*41*). We analyzed the decadal variation of the Bjerknes feedback in the duration of early pIOD events (June to August). The results show that all the three components of Bjerknes feedback have strengthened in the past decades (Fig. 3, C to E; see the "Strength of Bjerknes feedback" section).

The thermocline-SST feedback is the key process of the Bjerknes feedback (*42*, *43*). Stronger-than-normal easterlies over Sumatra-Java and along the equatorial Indian Ocean lift the thermocline off the southeastern Indian Ocean to a depth whereby upwelling cools the SST. The cooling contributes to an anomalous west-minus-east SST gradient. Therefore, the subsurface temperature variations play an important role in inducing decadal changes in the pIOD frequency (*44*). The thermocline-SST feedback has increased in the past decades (Fig. 3C). This trend is caused by the decadal shoaling thermocline in the tropical eastern Indian Ocean (*5*, *41*, *42*, *45*). Shallower thermocline implies that the subsurface cold water is closer to the surface to influence the SST. Thus, there are increased SST variations for a given size of the thermocline displacement.

An anomalous west-minus-east SST gradient can lead to stronger easterlies over the equatorial Indian Ocean. The response of surface zonal winds is linked to convection and precipitation changes induced by SST variations (*46*, *47*). We find that the zonal wind–SST feedback gets slightly stronger in recent decades (Fig. 3D). The strengthened feedback is related to background warming, as the connection between SST and deep convection gets stronger over warmer SST (*43*).

An easterly equatorial wind anomaly may lift (suppress) the thermocline in the eastern (western) part of the basin, which results in the thermocline-equatorial zonal wind feedback. After the 1980s, the intensity of this feedback has increased substantially compared to the previous decades (Fig. 3E). It can probably be attributed to the decadal shoaling of the thermocline in the southeastern Indian Ocean (*42*). When the thermocline gets closer to the surface, the wind can force the thermocline more quickly and more directly.

According to the above analysis, the trigger of early pIOD events has become more active in the past few decades; moreover, the Bjerknes feedback has also strengthened. These changes together lead to the increase in early pIOD events.

Response of early pIOD to future greenhouse warming

To assess the influence of greenhouse warming on early pIOD events, we use outputs from 26 CMIP5 and 37 CMIP6 models in which the ocean temperature, surface wind, and precipitation data are available, covering the 2006–2100 and 2015–2100 periods. The coupled general circulation models (CGCMs) used in this study are
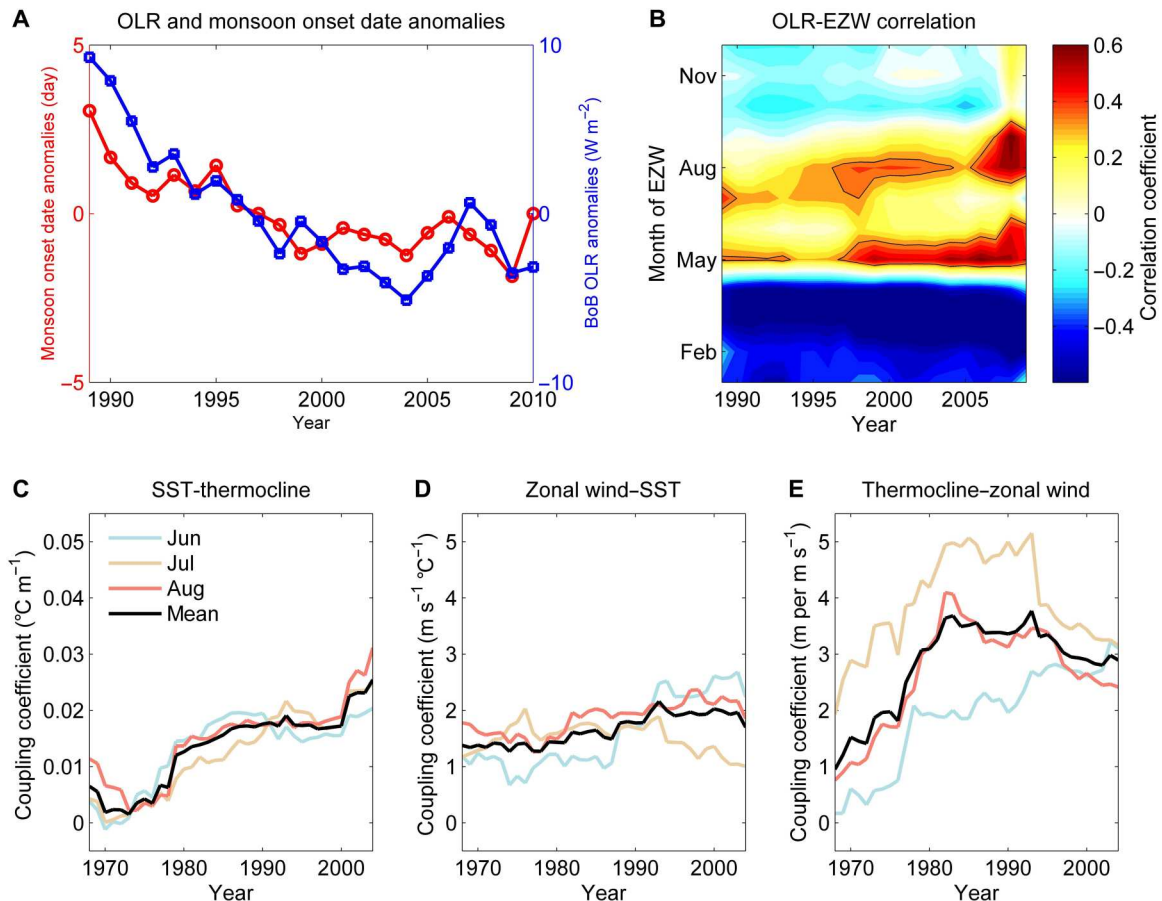
Fig. 3. Observed decadal variations of the influencing factors for early pIOD. (**A**) Twenty-one–year running mean of monsoon onset date anomalies (day; negative values indicate early monsoon onset; red line) in the BoB and 21-year running mean of OLR anomalies (W m^{-1}; blue line) in the BoB (7.5°N to 12.5°N, 85°E to 95°E) during monsoon onset stage (the fifth to sixth pentads of April and the first pentad of May). (**B**) Twenty-one–year moving correlation (shading) between the BoB OLR anomalies during monsoon onset stage and equatorial zonal wind (EZW; 5°S to 5°N, 40°E to 100°E) anomalies with positive results over 90% confidence level are enclosed by black contours. (**C**) Strength of SST-thermocline feedback (°C m^{-1}), (**D**) zonal wind–SST feedback (m s^{-1}°C^{-1}), and (**E**) thermocline–zonal wind feedback (m per m s^{-1}) in 31-year sliding periods (see the "Strength of Bjerknes feedback" section).

forced with future greenhouse gas emission scenarios of Representative Concentration Pathway 8.5 (RCP8.5) for CMIP5 and the equivalent updated scenario for CMIP6 [Shared Socioeconomic Pathway 5-8.5 (SSP5-8.5)]. Not all CGCMs are able to simulate the characteristics of observed early pIOD because the simulation of monsoon onset process, which is crucial for triggering early pIOD events, is problematic in CGCMs (*48*). We focus on the 16 CGCMs in which the observed spring-summer EEWA mode can be extracted by EOF analysis from the model simulations, and the early pIOD can be reasonably reproduced. The models are selected on the basis of objective criteria. In total, 6 CMIP5 models and 10 CMIP6 models are selected (fig. S4; see also the "Model selection" section). Early pIOD events simulated by selected models peak, on average, in August and decay in boreal fall, which is in agreement with the observational results (figs. S5 and S6). The spatial pattern of an early IOD event is also reasonably reproduced (fig. S7). The simulated early pIOD peaks and decays earlier and is smaller in magnitude compared with the IOD co-occurring with ENSO. These features are consistent with that from the observations. The

simulated IOD intensities of the two types of IODs are both comparable with the observed values (fig. S8).

We define early pIOD events in the same manner as for the observed events. A total of 12 of the 16 models simulate an increase in the frequency of early pIOD events. The multimodel mean frequency of early pIOD events increases by 73%, from 1.90 events every 31 years in the beginning of this century to 3.28 events in 31 years in the end of this century (Fig. 4A). The increasing trend is statistically significant according to an *F* test. Consistently, the PC of the simulated spring-summer EEWA mode increases continually in the same period (fig. S9).

As in observations, the increased occurrences of early pIOD under future greenhouse warming arise because of early summer monsoon onset. We compared the monsoon onset date in the first and last 25 years of the 2015–2100 period. Results show that 15 of 16 models simulate an early Indian summer monsoon onset under greenhouse warming (Fig. 4B; see the "Monsoon onset date" section).

Among the three components of the Bjerknes feedback, thermocline-SST feedback is the most important component and is most
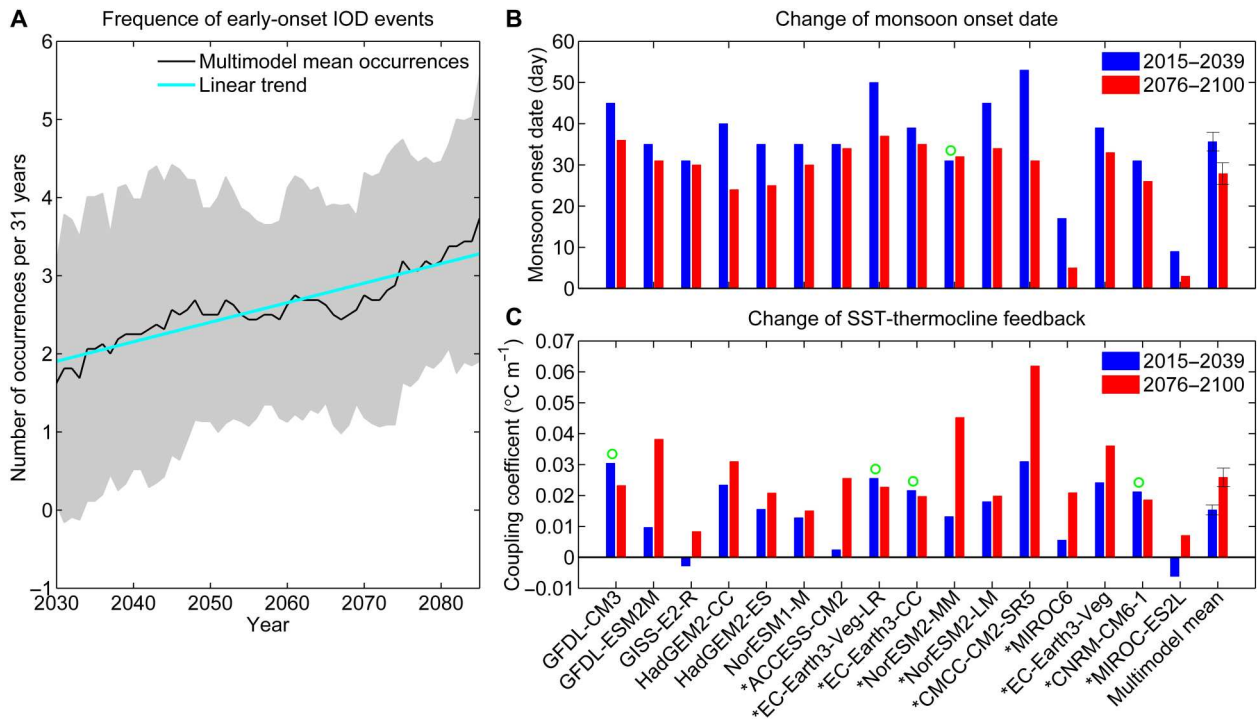
Fig. 4. Simulated changes in the frequency of early pIOD events and its influencing factors. (**A**) Simulated number of early pIOD events in 31-year sliding periods under future greenhouse warming. The black line indicates the multimodel mean results. The blue line indicates the linear trend of multimodel mean results. The 1 SD among models is shaded. (**B**) Indian summer monsoon onset date over the first (2015–2039, blue bars) and last (2076–2100, red bars) 25 years of the simulations. Onset date is counted from 10 May. The error bar in the multimodel mean represents the 95% confidence level determined by a bootstrap test. Fifteen of 16 selected models generate an advance in monsoon onset date under future greenhouse warming, except for one model generating a delay (indicated by green circle). The multimodel mean advance in monsoon onset date is statistically significant above the 95% confidence level. (**C**) Simulated strength of SST-thermocline feedback (°C m^{-1}; June to August) over the first (2015–2039, blue bars) and last (2076–2100, red bars) 25 years of the simulations. The error bar in the multimodel mean represents the 95% confidence level determined by a bootstrap test. Twelve of 16 selected models generate an increase in coupling strength under future greenhouse warming, except for 4 models generating a decrease (indicated by green circles). The multimodel mean increase is statistically significant above the 95% confidence level. Models from CMIP6 are indicated by asterisks.

crucial for IOD development (*49*). It intensifies markedly by 69% under global warming (Fig. 4C), which is significant above the 95% confidence level determined by a bootstrap test (see the "Statistical significance test" section). The intensification of this feedback arises from mean state changes in the Indian Ocean. The climatological thermocline in the eastern Indian Ocean shallows in CGCMs under global warming because of the weakened Walker circulation (*23*, *42*), which provides a favorable condition for SST response to the thermocline. It is reported that the thermocline in the eastern Indian Ocean is too shallow in the CMIP simulations, which may lead to too strong thermocline-SST feedback (*50*, *51*). We analyzed the change of thermocline-SST feedback under future global warming in the nonselected models. The result shows no intermodel consensus, and the multimodel mean change is not statistically significant (fig. S10). This is in sharp contrast to the result using the selected models, which simulate a significant increase in the strength of thermocline-SST feedback (Fig. 4C). This result provides evidence for importance of enhanced thermocline-SST feedback in the increased occurrences of early IOD events.

The feedback between zonal wind and SST experiences a weak decrease (15%) under global warming, which is also significant according to bootstrap test (fig. S11). The static stability of the troposphere increases under future warming, which weakens the wind response to SST variations (*42*, *45*). Moreover, the change of thermocline–zonal wind feedback is insignificant (fig. S12). In general, the overall strength of Bjerknes feedback is enhanced under global warming, contributing to the development of initial anomalies caused by the early summer monsoon onset.

DISCUSSION

In summary, the pIOD frequency has increased significantly since the 1990s, but the dominant type has also changed substantially. The early pIOD, which was rarely seen in the 20th century, has become a major type of the pIOD in the 21st century and will likely become even more frequent in the future. Not all models can reasonably simulate the spring-summer EEWA mode, which are tightly correlated with the early pIOD. However, the models by which this mode is reproduced show an increasing trend of early pIOD frequency congruously. In addition, the underlying mechanisms for this increasing trend are consistent with that found in observations. The consistency of the results in observations and simulations supports our conclusion that the increase of early pIOD is associated with early summer monsoon onset and enhanced Bjerknes feedback. The increased occurrences of early pIOD events could intensify climate variability during boreal summer,

leading to more frequent extreme climate events with profound consequences for the society and economy of the surrounding Indian Ocean countries. The results of this study advance our understanding in IOD decadal variability and will contribute to better prediction and climate projection of the IOD and its related climate anomalies.

MATERIALS AND METHODS
Data
The wind data used in this study are monthly data at 850 hPa from the fifth generation ECMWF reanalysis (ERA5), the latest climate reanalysis produced by the European Center for Medium-Range Weather Forecasts [https://www.ecmwf.int/en/research/climate-reanalysis, (*52*)]. Wind anomalies are calculated with respect to the mean of 1979–2020 data. Monthly mean 850-hPa wind data from the National Centers for Environmental Prediction/National Center for Atmospheric Research (NCEP/NCAR) reanalysis (*53*) are also used. NCEP/NCAR wind anomalies are calculated with respect to the mean of 1948–2020 data. The 850-hPa wind is used because it is more suitable for studying the variations of the Indian summer monsoon and it is highly correlated with the surface wind, which could directly force the IOD. The UK Meteorological Office Hadley Center EN4.2.1 quality-controlled ocean temperature datasets (*54*) are used to study subsurface temperature variations. Temperature anomalies are calculated with respect to the mean of 1948–2020 data. Monthly SST data from National Oceanic and Atmospheric Administration (NOAA) Extended Reconstructed Sea Surface Temperature version 5 (ERSSTv5) are also used (*55*). The daily average, monthly mean, and long-term mean of OLR are calculated from the NOAA interpolated OLR product (*56*). The OLR anomaly is used as a proxy for large-scale convective activity over the Indian Ocean. The OLR anomaly is calculated with respect to the long-term mean of 1979–2020 data.

EOF analysis
An EOF analysis is used to identify the dominant modes of equatorial zonal wind interannual variability. We apply the EOF analysis on the time series of ERA5 equatorial zonal wind anomaly (averaged between 5°S and 5°N) yearly evolution from 1948 to 2020, in which the two-dimensional spatial part is the seasonal evolution of zonal wind of individual years (January to December), and the temporal dimension is the years from 1948 to 2020 (fig. S1). The linear trend is removed before calculation. The results are similar when the NCEP/NCAR data are used for EOF analysis (fig. S2). The most notable feature of the first leading mode (EOF1) is that the EEWA peaks in fall. This feature is very similar to the EEWA evolution pattern during canonical pIOD events (Fig. 1E). We refer to EOF1 as the fall EEWA mode. The second leading mode (EOF2) shows an EEWA that sets up in May and persists through spring and summer. We refer to EOF2 as the spring-summer EEWA mode. The pattern of EOF2 well represents the evolution of EEWA during early pIOD events (Fig. 1B).

Occurrences of pIOD events
The DMI is represented by the difference in SSTA between the tropical western Indian Ocean (10°S to 10°N, 50°E to 70°E) and the tropical southeastern Indian Ocean (10°S to 0°, 90°E to 110°E). Different from the SSTA at the eastern Indian Ocean that is manifested only

south of the equator, the thermocline depth anomalies are very symmetric about the equator (*8*). Therefore, the thermocline DMI is defined as the difference in thermocline depth (depth of the 20°C isotherm) anomalies between 5°S to 5°N, 50°E to 70°E and 5°S to 5°, 90°E to 105°E. Because early pIOD events cannot be distinguished from canonical pIOD events by DMI only, we distinguish different types of pIOD events with the help of the Niño 3.4 index and the results of EOF analysis. The Niño 3.4 index in a certain year is represented by the average value from December to next February, and the DMI is represented by the July to October averages of the DMI, with the linear trend being removed. An early pIOD event is determined when DMI and the PC2 (time series of spring-summer EEWA mode based on NCEP/NCAR data, which has a longer time span than ERA5) are both greater than 0.75 SD. PIOD co-occurring with ENSO is defined as occurring when the DMI and the Niño 3.4 index both exceed 0.75 SD.

We constructed an ENSO-independent residual of DMI by removing the common influence of ENSO. The expected influence of ENSO is represented by the linear regression of DMI averaged in July to October onto the Niño 3.4 index in the same months.

Strength of Bjerknes feedback
We use a zonal wind–SST coupling coefficient to represent how strong the low-level wind responds to a unit SSTA forcing. It is measured by the slope in the scatter diagrams between the SSTA in the southeastern Indian Ocean (10°S to 0°, 90°E to 110°E), where the strongest SSTA occur, and the zonal wind anomaly in the central equatorial Indian Ocean (5°S to 5°N, 70°E to 90°E). The linear slope was calculated on the basis of the least squares fitting method.

We use a thermocline–zonal wind coupling coefficient to represent the strength of thermocline depth change for a given unit zonal wind forcing. It can be represented by the slope in the scatter diagrams between the zonal wind anomalies in the central Indian Ocean (5°S to 5°N, 70°E to 90°E) and the thermocline depth anomalies in the southeastern Indian Ocean (10°S to 0°, 90°E to 110°E).

We use an SST-thermocline coupling coefficient to represent how strong the SST responds to a unit thermocline depth displacement. Mathematically, it equals the linear slope of scatter diagram of thermocline depth anomalies and SSTA in the southeastern Indian Ocean (10°S to 0°, 90°E to 110°E).

In all the scatterplots used for feedback strength calculation, the independent variable is the abscissa and the dependent variable is the ordinate. We calculate the variability of feedback strength under a 31-year sliding window. Decadal signals are removed by subtracting the 11-year running mean from the monthly anomalies before calculating the strength of Bjerknes feedback.

Monsoon onset date
The observed onset date of summer monsoon in the BoB is defined on the basis of both convection and zonal wind (*34*). That is, the OLR values in the central BoB (7.5°N to 12.5°N, 85°E to 95°E) must be lower than 220 W m^{-2}, and the westerly zonal wind in the same area must be persistent for more than two pentads. Considering that the CGCM simulations of intraseasonal variability and convection remains problematic in individual models (*48*), the simulated Indian summer monsoon onset date is determined using only precipitation data with reference to previous studies (*57*–*60*). The monsoon domain is defined where the annual range of precipitation exceeds 2.5 mm day^{-1}. The annual range is defined as the

difference between the May to September mean and the November to March mean precipitation. The onset date is calculated on the basis of the relative climatological mean daily precipitation, which is the difference between the climatological daily precipitation and dry month (January) mean precipitation. The daily climatology of precipitation is defined as the sum of the first 12 harmonics of daily average precipitation. The onset date is defined as the date when the relative precipitation averaged in the monsoon domain first exceeds 6 mm day^{-1}.

Model selection

We use the outputs from 26 CMIP5 and 37 CMIP6 models in which the ocean temperature, surface wind, and precipitation data are available, covering the 2006–2100 and 2015–2100 periods, respectively. The CGCMs are forced with future greenhouse gases under RCP8.5 for CMIP5 and SSP5-8.5 for CMIP6. All the CGCMs can well reproduce the fall EEWA modes as the dominant mode. However, not all the CGCMs are able to simulate the spring-summer EEWA mode. Given that the spring-summer EEWA that associate with early monsoon onset is essential for the development of early pIOD, we select models in which the spring-summer EEWA mode can be reasonably reproduced. Then, we further test their capability in reproducing the seasonal cycle of early pIOD. The objective criteria are as follows. First, the observed and simulated spring-summer EEWA mode patterns are significantly correlated above the 99% confidence level. The observed and simulated EOF patterns are zonally averaged before analysis. Second, EEWA in the spring-summer EEWA mode persists through spring and summer (May to August). Third, the DMI associated with the spring-summer EEWA mode (obtained by a linear regression onto the corresponding PC) shows similar seasonal evolution with observed early pIOD (positive DMI persists through June to September and peaks between July and September). Under these criteria, a total of 6 CMIP5 models (GFDL-CM3, GFDL-ESM2M, GISS-E2-R, HadGEM2-CC, HadGEM2-ES, and NorESM1-M) and 10 CMIP6 models (ACCESS-CM2, EC-Earth3-Veg-LR, EC-Earth3-CC, NorESM2-MM, NorESM2-LM, CMCC-CM2-SR5, MIROC6, EC-Earth3-Veg, CNRM-CM6-1, and MIROC-ES2L) are selected.

Monthly anomalies are calculated by subtracting the climatology in each model. The EOF analysis of EEWA is calculated using the same method as that in observations. The linear trend is removed before calculation. Considering that the 20°C isotherm fail to reflect the realistic long-term trend of thermocline depth under the circumstance of a climate shift (61), the thermocline depth is defined as the depth of the maximum vertical temperature gradient when analyzing the CMIP5 and CMIP6 simulations.

Statistical significance test

We use a bootstrap method (62) to examine the significance of results. The samples of the monsoon onset date from the 16 selected models are resampled randomly to construct 10,000 realizations. In the random resampling process, any monsoon onset date is allowed to be selected again. The SD of the 10,000 inter-realizations is 2.2415 days for the monsoon onset date in the period of 2015–2039, while it is 2.6277 days for the period of 2076–2100. The monsoon onset date gets earlier for 7.75 days in multimodel mean, which is greater than the sum of the two SD values, indicating that the statistical significance is above the 95% confidence level.

The same test is carried out for the change in Bjerknes feedback strength between the periods of the first and last 25 years of the simulations. The SD of the inter-realization is 0.0016 and 0.0029°C m^{-1} for the coupling coefficient of SST-thermocline feedback in the periods of 2015–2039 and 2076–2100, respectively. The multimodel mean increase (0.0105°C m^{-1}) is greater than the sum of the two SD values, indicating the statistical significance above the 95% confidence level. The SD of inter-realization is 0.0768 and 0.0737 m s^{-1}°C^{-1} for the coupling coefficient of zonal wind–SST feedback in the two periods. The multimodel mean decrease (0.2692 m s^{-1}°C^{-1}) is greater than the sum of the two SD values, indicating the statistical significance above the 95% confidence level. The SD of the 10,000 inter-realizations is 0.3265 and 0.2498 m per m s^{-1} for the coupling coefficient of thermocline–zonal wind feedback in the two periods. The multimodel mean decrease (0.4223 m per m s^{-1}) is smaller than the sum of the two SD values, indicating that the decrease is not significant at the 95% confidence level.

REFERENCES AND NOTES

1. N. Saji, B. Goswami, P. Vinayachandran, T. Yamagata, A dipole mode in the tropical Indian Ocean. *Nature* **401**, 360–363 (1999).
2. P. J. Webster, A. M. Moore, J. P. Loschnigg, R. R. Leben, Coupled ocean–atmosphere dynamics in the Indian Ocean during 1997–98. *Nature* **401**, 356–360 (1999).
3. F. A. Schott, S. P. Xie, J. P. McCreary Jr., Indian Ocean circulation and climate variability. *Rev. Geophys.* **47**, RG1002 (2009).
4. N. J. Abram, M. K. Gagan, J. E. Cole, W. S. Hantoro, M. Mudelsee, Recent intensification of tropical climate variability in the Indian Ocean. *Nat. Geosci.* **1**, 849–853 (2008).
5. K. Ashok, W.-L. Chan, T. Motoi, T. Yamagata, Decadal variability of the Indian Ocean dipole. *Geophys. Res. Lett.* **31**, L24207 (2004).
6. K. Ashok, Z. Guan, T. Yamagata, Impact of the Indian Ocean dipole on the relationship between the Indian monsoon rainfall and ENSO. *Geophys. Res. Lett.* **28**, 4499–4502 (2001).
7. K. Ashok, Z. Guan, T. Yamagata, Influence of the Indian Ocean Dipole on the Australian winter rainfall. *Geophys. Res. Lett.* **30**, 1821 (2003).
8. N. Saji, The Indian Ocean Dipole. *Oxford Research Encyclopedia of Climate Science* , (Oxford Univ. Press, 2018).
9. G. Wang, W. Cai, Two-year consecutive concurrences of positive Indian Ocean Dipole and central Pacific El Niño preconditioned the 2019/2020 Australian "black summer" bushfires. *Geosci. Lett.* **7**, 19 (2020).
10. W. Cai, A. Santoso, G. Wang, E. Weller, L. Wu, K. Ashok, Y. Masumoto, T. Yamagata, Increased frequency of extreme Indian Ocean Dipole events due to greenhouse warming. *Nature* **510**, 254–258 (2014).
11. W. Cai, K. Yang, L. Wu, G. Huang, A. Santoso, B. Ng, G. Wang, T. Yamagata, Opposite response of strong and moderate positive Indian Ocean Dipole to global warming. *Nat. Clim. Chang.* **11**, 27–32 (2021).
12. S. Endo, T. Tozuka, Two flavors of the Indian Ocean Dipole. *Clim. Dynam.* **46**, 3371–3385 (2016).
13. Y. Du, W. Cai, Y. Wu, A new type of the Indian Ocean Dipole since the mid-1970s. *J. Clim.* **26**, 959–972 (2013).
14. E. Weller, W. Cai, Y. Du, S. K. Min, Differentiating flavors of the Indian Ocean Dipole using dominant modes in tropical Indian Ocean rainfall. *Geophys. Res. Lett.* **41**, 8978–8986 (2014).
15. S. Sun, J. Lan, Y. Fang, Tana, X. Gao, A triggering mechanism for the Indian Ocean dipoles independent of ENSO. *J. Clim.* **28**, 5063–5076 (2015).
16. N. Anil, M. R. Ramesh Kumar, R. Sajeev, P. K. Saji, Role of distinct flavours of IOD events on Indian summer monsoon. *Nat. Hazards* **82**, 1317–1326 (2016).
17. H. Annamalai, R. Murtugudde, J. Potemra, S. P. Xie, P. Liu, B. Wang, Coupled dynamics over the Indian Ocean: Spring initiation of the zonal mode. *Deep Sea Res. Part II Top. Stud. Oceanogr.* **50**, 2305–2330 (2003).

18. T. Li, B. Wang, C. P. Chang, Y. Zhang, A theory for the Indian Ocean Dipole–zonal mode. *J. Atmos. Sci.* **60**, 2119–2135 (2003).

19. C. C. Hong, M. M. Lu, M. Kanamitsu, Temporal and spatial characteristics of positive and negative Indian Ocean dipole with and without ENSO. *J. Geophys. Res. Atmos.* **113**, D08107 (2008).

20. T. Yamagata, S. K. Behera, S. A. Rao, Z. Guan, K. Ashok, H. N. Saji, Comments on "dipoles, temperature gradients, and tropical climate anomalies". *Bull. Am. Meteorol. Soc.* **84**, 1418–1422 (2003).

21. S. A. Rao, S. K. Behera, Y. Masumoto, T. Yamagata, Interannual subsurface variability in the tropical Indian Ocean with a special emphasis on the Indian Ocean Dipole. *Deep Sea Res. II Top. Stud. Oceanogr.* **49**, 1549–1572 (2002).

22. K. Ashok, Z. Guan, T. Yamagata, A look at the relationship between the ENSO and the Indian Ocean Dipole. *J. Meteorol. Soc. Japan. Ser. II* **81**, 41–56 (2003).

23. P. N. DiNezio, M. Puy, K. Thirumalai, F. F. Jin, J. E. Tierney, Emergence of an equatorial mode of climate variability in the Indian Ocean. *Sci. Adv.* **6**, eaay7684 (2020).

24. S. Marathe, P. Terray, A. Karumuri, Tropical Indian Ocean and ENSO relationships in a changed climate. *Clim. Dyn.* **56**, 3255–3276 (2021).

25. Y. Zhang, Y. Du, S. Zheng, Y. Yang, X. Cheng, Impact of Indian Ocean Dipole on the salinity budget in the equatorial Indian Ocean. *J. Geophys. Res. Ocean.* **118**, 4911–4923 (2013).

26. W. Cai, A. Sullivan, T. Cowan, How rare are the 2006–2008 positive Indian Ocean Dipole events? An IPCC AR4 climate model perspective. *Geophys. Res. Lett.* **36**, 08702 (2009).

27. W. Cai, A. Sullivan, T. Cowan, Climate change contributes to more frequent consecutive positive Indian Ocean Dipole events. *Geophys. Res. Lett.* **36**, L23704 (2009).

28. J. J. Luo, S. Behera, Y. Masumoto, H. Sakuma, T. Yamagata, Successful prediction of the consecutive IOD in 2006 and 2007. *Geophys. Res. Lett.* **35**, L14S02 (2008).

29. K. E. Taylor, R. J. Stouffer, G. A. Meehl, An overview of CMIP5 and the experiment design. *Bull. Am. Meteorol. Soc.* **93**, 485–498 (2012).

30. V. Eyring, S. Bony, G. A. Meehl, C. A. Senior, B. Stevens, R. J. Stouffer, K. E. Taylor, Overview of the coupled model intercomparison project phase 6 (CMIP6) experimental design and organization. *Geosci. Model Dev.* **9**, 1937–1958 (2016).

31. B. Wang, Q. Ding, P. V. Joseph, Objective definition of the Indian summer monsoon onset. *J. Climate* **22**, 3303–3316 (2009).

32. H. K. L. Drbohlav, S. Gualdi, A. Navarra, A diagnostic study of the Indian Ocean Dipole mode in El Niño and non–El Niño years. *J. Climate* **20**, 2961–2977 (2007).

33. T. Shinoda, M. A. Alexander, H. H. Hendon, Remote response of the Indian Ocean to interannual SST variations in the tropical Pacific. *J. Climate* **17**, 362–372 (2004).

34. W. D. Yu, K. P. Li, J. W. Shi, L. Liu, H. W. Wang, Y. L. Liu, The onset of the monsoon over the Bay of Bengal: The year-to-year variations. *Atmos. Ocean. Sci. Lett.* **5**, 342–347 (2012).

35. B. Xiang, B. Wang, Mechanisms for the advanced Asian summer monsoon onset since the mid-to-late 1990s. *J. Climate* **26**, 1993–2009 (2013).

36. B. Wang, Z. Fan, Choice of south Asian summer monsoon indices. *Bull. Am. Meteorol. Soc.* **80**, 629–638 (1999).

37. H. H. Hsu, C. T. Terng, C. T. Chen, Evolution of large-scale circulation and heating during the first transition of Asian summer monsoon. *J. Climate* **12**, 793–810 (1999).

38. K. Li, W. Yu, T. Li, V. S. N. Murty, S. Khokiattiwong, T. R. Adi, S. Budi, Structures and mechanisms of the first-branch northward-propagating intraseasonal oscillation over the tropical Indian Ocean. *Climate Dynam.* **40**, 1707–1720 (2013).

39. Y. Kajikawa, T. Yasunari, S. Yoshida, H. Fujinami, Advanced Asian summer monsoon onset in recent decades. *Geophys. Res. Lett.* **39**, L03803 (2012).

40. J. Bjerknes, Atmospheric teleconnections from the equatorial Pacific. *Mon. Weather Rev.* **97**, 163–172 (1969).

41. L. Liu, W. Yu, T. Li, Dynamic and thermodynamic air-sea coupling associated with the Indian Ocean Dipole diagnosed from 23 WCRP CMIP3 models. *J. Climate* **24**, 4941–4958 (2011).

42. W. Cai, X. T. Zheng, E. Weller, M. Collins, T. Cowan, M. Lengaigne, W. Yu, T. Yamagata, Projected response of the Indian Ocean Dipole to greenhouse warming. *Nat. Geosci.* **6**, 999–1007 (2013).

43. J. F. Lübbecke, M. J. McPhaden, Assessing the twenty-first-century shift in ENSO variability in terms of the Bjerknes stability index. *J. Climate* **27**, 2577–2587 (2014).

44. F. Feba, K. Ashok, M. Collins, S. R. Shetye, Emerging skill in multi-year prediction of the Indian Ocean Dipole. *Front. Clim.* **3**, 736759 (2021).

45. X. T. Zheng, S. P. Xie, G. A. Vecchi, Q. Liu, J. Hafner, Indian Ocean Dipole response to global warming: Analysis of ocean-atmospheric feedbacks in a coupled model. *J. Climate* **23**, 1240–1253 (2010).

46. A. E. Gill, Some simple solutions for heat-induced tropical circulation. *Q. J. Roy. Meteorol. Soc.* **106**, 447–462 (1980).

47. R. S. Lindzen, S. Nigam, On the role of sea surface temperature gradients in forcing low-level winds and convergence in the tropics. *J. Atmos. Sci.* **44**, 2418–2436 (1987).

48. K. R. Sperber, H. Annamalai, I. S. Kang, A. Kitoh, A. Moise, A. Turner, B. Wang, T. Zhou, The Asian summer monsoon: An intercomparison of CMIP5 vs. CMIP3 simulations of the late 20th century. *Climate Dynam.* **41**, 2711–2744 (2013).

49. A. Deshpande, J. S. Chowdary, C. Gnanaseelan, Role of thermocline–SST coupling in the evolution of IOD events and their regional impacts. *Climate Dynam.* **43**, 163–174 (2014).

50. W. Cai, T. Cowan, Why is the amplitude of the Indian Ocean Dipole overly large in CMIP3 and CMIP5 climate models? *Geophys. Res. Lett.* **40**, 1200–1205 (2013).

51. G. Li, S. P. Xie, Y. Du, A robust but spurious pattern of climate change in model projections over the tropical Indian Ocean. *J. Climate* **29**, 5589–5608 (2016).

52. H. Hersbach, B. Bell, P. Berrisford, S. Hirahara, A. Horányi, J. Muñoz-Sabater, J. Nicolas, C. Peubey, R. Radu, D. Schepers, A. Simmons, C. Soci, S. Abdalla, X. Abellan, G. Balsamo, P. Bechtold, G. Biavati, J. Bidlot, M. Bonavita, G. De Chiara, P. Dahlgren, D. Dee, M. Diamantakis, R. Dragani, J. Flemming, R. Forbes, M. Fuentes, A. Geer, L. Haimberger, S. Healy, R. J. Hogan, E. Hólm, M. Janisková, S. Keeley, P. Laloyaux, P. Lopez, C. Lupu, G. Radnoti, P. de Rosnay, I. Rozum, F. Vamborg, S. Villaume, J. N. Thépaut, The ERA5 global reanalysis. *Q. J. Roy. Meteorol. Soc.* **146**, 1999–2049 (2020).

53. E. Kalnay, M. Kanamitsu, R. Kistler, W. Collins, D. Deaven, L. Gandin, M. Iredell, S. Saha, G. White, J. Woollen, Y. Zhu, M. Chelliah, W. Ebisuzaki, W. Higgins, J. Janowiak, K. C. Mo, C. Ropelewski, J. Wang, A. Leetmaa, R. Reynolds, R. Jenne, D. Joseph, The NCEP/NCAR 40-year reanalysis project. *Bull. Am. Meteorol. Soc.* **77**, 437–472 (1996).

54. S. A. Good, M. J. Martin, N. A. Rayner, EN4: Quality controlled ocean temperature and salinity profiles and monthly objective analyses with uncertainty estimates. *J. Geophys. Res. Ocean.* **118**, 6704–6716 (2013).

55. B. Huang, P. W. Thorne, V. F. Banzon, T. Boyer, G. Chepurin, J. H. Lawrimore, M. J. Menne, T. M. Smith, R. S. Vose, H. M. Zhang, Extended reconstructed sea surface temperature, version 5 (ERSSTv5): Upgrades, validations, and intercomparisons. *J. Climate* **30**, 8179–8205 (2017).

56. B. Liebmann, C. A. Smith, Description of a complete (interpolated) outgoing longwave radiation dataset. *Bull. Am. Meteorol. Soc.* **77**, 1275–1277 (1996).

57. B. Wang, LinHo, Rainy season of the Asian-Pacific summer monsoon. *J. Climate* **15**, 386–398 (2002).

58. B. Wang, H. J. Kim, K. Kikuchi, A. Kitoh, Diagnostic metrics for evaluation of annual and diurnal cycles. *Climate Dynam.* **37**, 941–955 (2011).

59. K. M. Lau, S. Yang, Climatology and interannual variability of the southeast asian summer monsoon. *Adv. Atmos. Sci.* **14**, 141–162 (1997).

60. A. Kitoh, H. Endo, K. Krishna Kumar, I. F. A. Cavalcanti, P. Goswami, T. Zhou, Monsoons in a changing world: A regional perspective in a global context. *J. Geophys. Res. Atmos.* **118**, 3053–3065 (2013).

61. H. Yang, F. Wang, Revisiting the thermocline depth in the equatorial Pacific. *J. Climate* **22**, 3856–3863 (2009).

62. P. C. Austin, J. V. Tu, Bootstrap methods for developing predictive models. *Am. Stat.* **58**, 131–137 (2004).